Self-Assembled, Nanowire Network Electrodes for Depleted Bulk Heterojunction Solar Cells

Xinzheng Lan, Jing Bai, Silvia Masala, Susanna M. Thon, Yuan Ren, Illan J. Kramer, Sjoerd Hoogland, Arash Simchi, Ghada I. Koleilat, Daniel Paz-Soldan, Zhijun Ning, André J. Labelle, Jin Young Kim, Ghassan Jabbour,* and Edward H. Sargent*

Since the first reports in 2005, colloidal quantum dot (CQD) solar cells have attracted growing attention in light of their ease of fabrication, their potential for low-cost manufacture, and their prospects for high efficiency enabled by quantum-size-effect-tuning to match their absorption with the sun's broad spectrum.[1–7] In this same period, performance has increased to reach certified solar power conversion efficiencies of 7%.[8] The quantum dot solids responsible for absorption and charge extraction have advanced thanks to improved passivation and densification, leveraging a combination of organic- and inorganic-ligand strategies. Improvements to device architecture have also played a major role, with the transition from the earlier Schottky structure to a depleted heterojunction (DH) enabling increased efficiency of photo-generated charge extraction.[9]

Nevertheless, existing CQD solar cells continue to deliver well under the ~36 mA/cm^2 of short-circuit current density of which their choice of bandgap should, in principle, make them capable.[10] Today, the absorption length ($1/\alpha$) at the exciton wavelength considerably exceeds the minority carrier diffusion length,[11,12] leading to an absorption–extraction compromise.

Depleted bulk heterojunction (DBH) solar cells have, therefore, attracted attention in light of their potential to help overcome this trade-off. Incorporating quantum dots into a porous TiO$_2$ electron acceptor enhances currents;[13] and the use of TiO$_2$ nanopillars, fabricated with the aid of an electron-beam-lithography-defined template,[14] allows further increase in rational understanding of the conditions under which the DBH architecture can lead to gains in performance.

Here we report a depleted bulk heterojunction, colloidal quantum dot solar cell that relies instead on a bottom-up synthesized, nanostructured TiO$_2$ electrode. We find that the growth mode of ZnO nanowires (NWs) provides the most morphologically optimal template for the nanostructured electrode; but that the electronic surface behaviour of TiO$_2$ is best for efficient current extraction and high open-circuit voltage (V_{OC}).[15,16] For this reason, we develop a bottom-up electrode fabrication technique that begins with a ZnO scaffold and that converts this template to TiO$_2$ while substantially retaining the morphology of the original structure. Averaging across thirty solar cells we obtained, using the nanowire network devices, static short-circuit current densities of 22.5 ± 0.9 mA/cm^2 and static air mass 1.5 (AM 1.5) power conversion efficiencies of 7.3 ± 0.2%. The solar power conversion efficiency measurements employed herein have a systematic error of less than 7% (see Experimental Section).

Figure 1a–c depicts the formation of the TiO$_2$ nanowire network (NWN) electrodes featured in this work. First, high-density ZnO NWs were synthesized via a hydrothermal process.[17,18] Second, liquid´-phase deposition (LPD) was used to treat the NWs. The LPD process involves hydrolysis of ammonium hexafluorotitanate,[19] leading to deposition of TiO$_2$ as well as mild etching of ZnO as a result of formation of HF. Due to surface tension during the evaporation of the solvent, the treatment of the NWs leads to partial connectivity among the constituent wires while retaining distinct pores open for subsequent infiltration. As a third step, TiCl$_4$ treatment was applied to the as-formed TiO$_2$ networks to convert the hollow tubes to rods and to optimize the electronic properties of the surface.

High-magnification scanning electron microscope (SEM) images (Figure S1a,b of the Supporting Information(SI)) of LPD-treated NWs before and after TiCl$_4$ treatment reveal porous tubular structures that become filled only with the benefit of the further step of TiCl$_4$ treatment. Transmission electron microscopy (TEM) images of LPD-treated NWs before and after TiCl$_4$ treatment (Figure S1c,d of the SI) confirm this

X. Lan,[+] Dr. J. Bai,[+] Dr. S. M. Thon, Dr. Y. Ren, Dr. I. J. Kramer,
Dr. S. Hoogland, Dr. A. Simchi, Dr. G. I. Koleilat, D. Paz-Soldan,
Dr. Z. Ning, A. J. Labelle, Dr. J. Y. Kim, Prof. E. H. Sargent
Department of Electrical and Computer Engineering
University of Toronto
10 King's College Road, Toronto, Ontario, M5S 3G4, Canada
E-mail: ted.sargent@utoronto.ca
X. Lan
School of Materials Science and Engineering
Hefei University of Technology
193 Tunxi Rd, Hefei, Anhui Province, 230009, P.R. China

Prof. G. Jabbour, Dr. S. Masala[+]
King Abdullah University of Science and Technology
4700 Thuwal 23955-6900 Saudi Arabia
E-mail: ghassan.jabbour@kaust.edu.sa
Dr. A. Simchi
Department of Materials Science and Engineering
Sharif University of Technology
P.O.Box 11365-9466, Azadi Avenue, Tehran, Iran
[+] X.L., J.B., and S.M. contributed equally to this work.
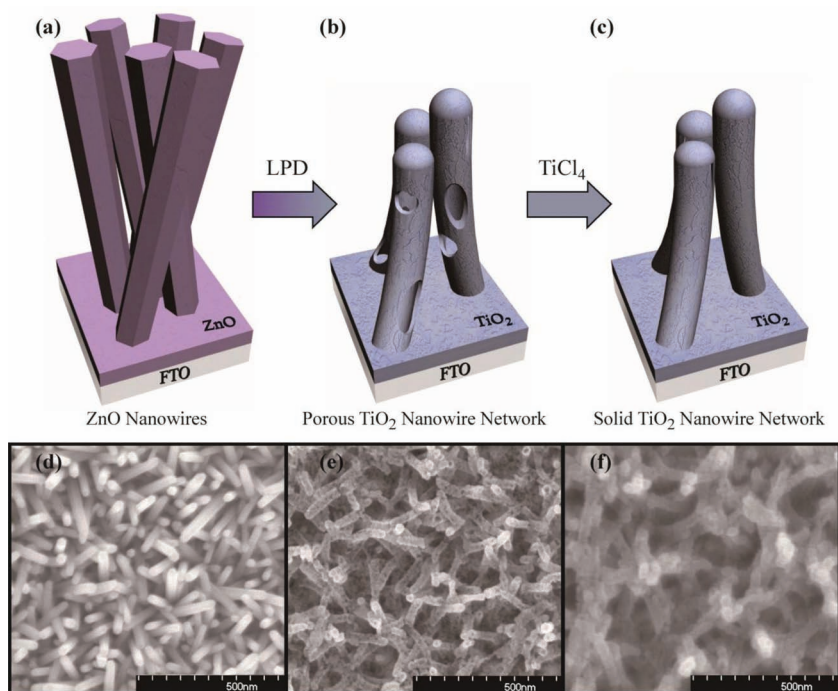
Figure 1. Optimized procedure to produce TiO_2 nanowire network (NWN) on F-doped SnO_2 (FTO) substrate. a,d) ZnO nanowires (NWs) were first synthesized on an FTO substrate via a hydrothermal method. b,e) ZnO NWs were converted to porous TiO_2 NWNs via liquid-phase deposition (LPD). c,f) Solid TiO_2 NWNs were formed as a result of $TiCl_4$ treatment.

interbundle separation was controlled by adjusting the density of the ZnO NWs. The growth of ZnO NWs includes two stages: heterogeneous nucleation and successive preferential growth along <001> direction. We found that density-controlled growth of ZnO NWs could be achieved by properly balancing heterogeneous nucleation and growth. This was achieved by changing the density of the ZnO seed and adding $NH_3 \cdot H_2O$. Figure S4c,d of the SI shows ZnO NW samples having different NW areal densities.

To explore whether the optimized NWN electrodes could promote improved solar cell performance, we built colloidal quantum dot photovoltaic devices and compared them to planar controls employing a TiO_2 electrode.[21] Using the NW growth and density control methods described above, we fabricated NW substrates with NW length of ~300 nm and interbundle separations of similar order (Figure 1f and Figure S3c of the SI), close to the ideal spacing predicted by the depletion width of our devices and diffusion length in our CQD films.[14] The thickness of the quantum dot layer was separately optimized on each electrode to maximize power conversion efficiency. The optimal quantum dot thickness was 320 ±10 nm for the planar electrode device, in good agreement with previous reports,[22] and 440 ±10 nm (including the fully infiltrated bottom NWN region) for the NWN electrode device (**Figure 3**). Between one third and one half of the quantum dot material lies within the network, with the remainder forming a planarizing overcoating (Figure 3a). Increasing the NW length beyond 300 nm led to an increased series resistance and decreased performance (Figure S5 of the SI).

finding: the hollow structure is seen in LPD-treated NWs, while the tubular structure is absent following $TiCl_4$ treatment. Energy-dispersive X-ray spectrometry (EDX) spectra of NWs at different fabrication stages, shown in Figure S2 of the SI, indicate that no Zn remains following the LPD process, consistent with complete conversion of ZnO into TiO_2 as a result of the LPD stage.

In developing the template-assisted nanowire network process, we found that the morphology of the NWs depends sensitively on the LPD process. Without LPD, all NWs were etched away (**Figure 2**a), attributable to uncontrolled hydrolysis that occurs during $TiCl_4$ in a highly acidic aqueous solution. LPD treatment employing moderate acidity solutions led to the desired formation of dense networks of hollow TiO_2 nanowires in a manner that substantially maintained the morphology of the template (Figure 1e). Too gentle a process, however, led to formation of undesired ZnO/TiO_2 core/shell structures (Figure 2b) that prevent the full conversion of the electrode into TiO_2,[20] compromising the desired electronic properties of the electrode. LPD over-treatment (Figure 2c) etched the NWs, leading to the formation of a quasi-planar electrode and to exposure of the underlying FTO substrate. The concentrations and treatment times required a systematic optimization then implemented in the optimized electrode fabrication protocol (see Experimental Section).

The length and density of the NWs also required optimization. The length of wires in the NWN was controlled by changing the length of the starting ZnO NWs, programmed via growth time. The resultant ZnO NWs of different lengths are shown in Figure S3a and Figure S4a,b in the SI. The

Figure 4a shows the double-pass absorption spectra for both NWN and planar devices. The optimized NWN device compared with the planar device, has enhanced optical absorption in the near infrared, where increased absorbance is most urgently needed. The external quantum efficiency spectrum (Figure 4b) shows that the increased absorption is successfully translated into a collected charge advantage—the internal quantum efficiency at the exciton is preserved as the absorption is enhanced going from planar to NWN electrodes.

We used capacitance–voltage measurements to investigate the origins of the improved efficiency. The intersection of the low-slope region of the C^{-2}–V curve (wherein further reverse-bias has little impact on the capacitance, hence on the extent of depletion, indicating substantially complete depletion) with the high-slope region of the C^{-2}–V curve (wherein increasing positive bias reduces the extent of the depletion region, increasing capacitance) lies in the positive-bias region, indicating that the NWN device can preserve essentially complete depletion even under operating photovoltaic (forward-biased) conditions characteristic of the maximum power point (Figure 4c). This is not true of a similarly thick planar device (Figure S6 of the SI).

Figure 4d shows the solar power conversion performance of a typical planar versus a typical NWN device. Static figures of
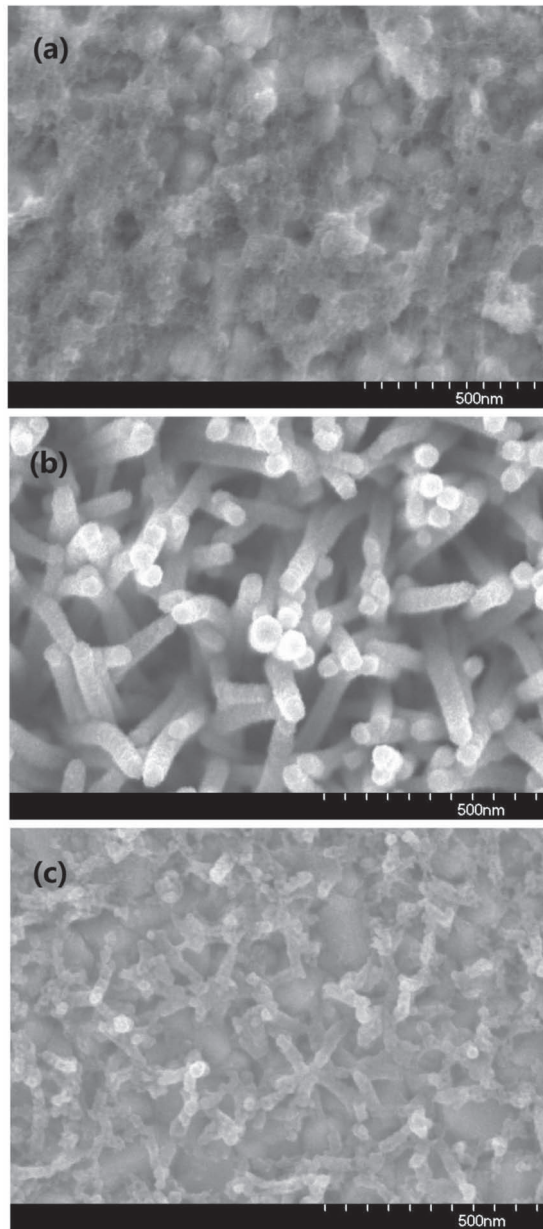
Figure 2. SEM images of ZnO NWs with different post-treatment: a) TiCl$_4$ treatment, b) soft LPD treatment, c) LPD overtreatment.
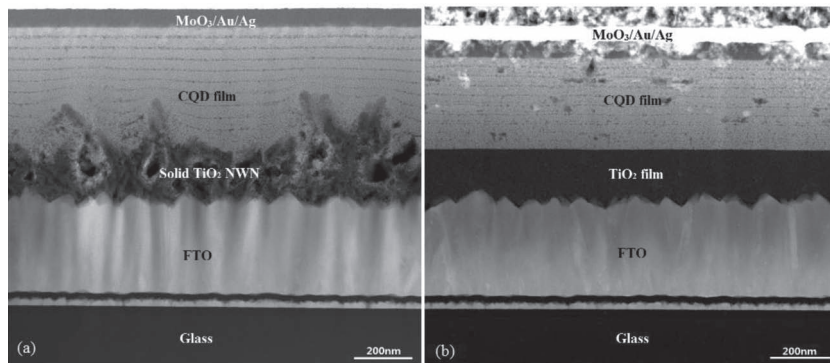
Figure 3. TEM images of a) optimized NWN device, and b) a planar device.

merit for both types of device are summarized in **Table 1**. The performance advance in the NWN device comes from an averaged increase of J_{sc} to 22.5 ± 0.9 mA/cm^2 compared with 19.8 ± 0.7 mA/cm^2 in the planar case. Integrating the EQE spectrum gives quantitative agreement with each reported short-circuit current density. The open-circuit voltage is the same in the planar and NWN devices confirming that the NWN process offers good control over interface states, a notable result given that the NWN electrode offers a considerably larger area of contact between the electrode and the quantum dot film.

In summary, we developed a solution-processed, bottom-up fabricated, nanowire network electrode that features a ZnO template converted into locally connected, yet infiltratable, TiO$_2$ nanowires. We used this new electrode to build a depleted bulk heterojunction solar cell employing hybrid-passivated colloidal quantum dots. The new electrode allowed us to apply a thicker, and thus, more light-absorbing, colloidal quantum dot active layer, from which we were able to obtain charge extraction with an efficiency comparable to that obtained from a thinner, planar device.

Experimental Section

ZnO NW Synthesis: The synthesis of ZnO NWs on FTO was performed following a two-step method. A ZnO seed layer was first formed on FTO-coated glass substrates by 3–5 iterations of spin-casting of a 5 mM zinc acetate solution in ethanol, followed by rapid crystallization at 400 °C for 20 minutes. This process was repeated twice to make sure conformal coating of the ZnO seed on FTO was achieved. Then, ZnO NW growth was carried out by suspending the seeded FTO substrate in a vertical manner in a container filled with an aqueous solution of zinc nitrate hydrate (0.025 M) and hexamethylenetetramine (0.025 M) at 90 °C. The reaction times were varied between 2 to 5 hours to produce NWs of the desired length. Following this reaction, the substrates were removed from solution, rinsed with DI water, and dried in air at 60 °C for 4 hours.

*LPD and TiCl$_4$ Treatment*: LPD treatment was conducted by placing ZnO NW substrates in a solution of 50 mM (NH$_4$)$_2$TiF$_6$ and 150 mM H$_3$BO$_3$ for 20 minutes at 25 °C. After LPD treatment, the NW substrates were thoroughly washed using DI water. Then, after drying at 60 °C, the treated NW substrates were sintered at 450 °C for 2 hours. TiCl$_4$ treatment was carried out by immersing LPD-treated NWs in an aqueous solution containing 120 mM TiCl$_4$ solution at 70 °C for 30 min. This treatment was followed by washing with DI water and drying. Finally, the samples were sintered at 500 °C for 30 minutes.

Device Fabrication and Characterization: The PbS CQD film was deposited in a layer-by-layer fashion by spin-casting. PbS CQDs in octane (50 mg/mL) were dispensed on the substrate and spin-cast at 2500 rpm for 10 seconds for each layer. A 1% v/v MPA:methanol solution was then dispensed to cover the entire substrate and spun after 3 seconds at the same speed for 5 seconds. Two rinses with methanol were applied for each layer.

The top electrode consisting of 15 nm of MoO$_3$, 50 nm of Au, and 120 nm of Ag was deposited by thermal (MoO$_3$ and Ag) and electron beam (Au) evaporation at a pressure of <1 × 10^{-6} Torr. The contact size defined by a shadow mask was 0.06 cm^2.

Optical absorption measurements were carried out in a Cary 500 UV-Vis-IR spectrophotometer using an integrating sphere.

J–V Characterization: AM 1.5 performance measurements were conducted using a class A
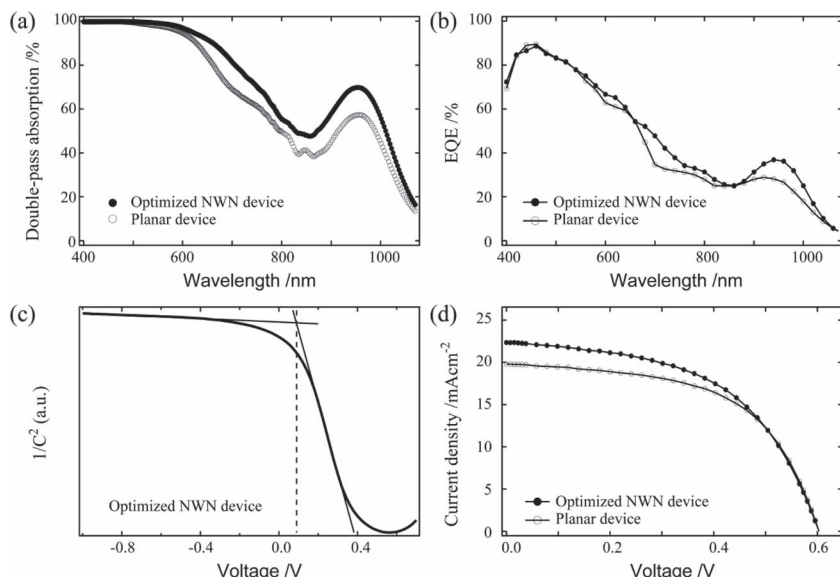
Figure 4. a) Double-pass optical absorption spectra of typical planar and NWN devices. b) External quantum efficiency spectra of the same devices. c) Capacitance^{-2} vs voltage curves for the NWN device showing that the device is substantially fully depleted even under slight forward bias. d) J–V curves under AM1.5 illumination of typical planar and NWN devices. The optimized NWN device shows the same open-circuit voltage as the planar counterpart, and a considerably increased photocurrent.

Table 1. Static figures of merit for both optimized NWN and planar devices. The statistics are based on thirty different devices. The solar power conversion efficiency measurements employed herein have a systematic error of less than 7% (see Experimental Section).

Device	V_{oc} [V]	J_{sc} [mA cm^{-2}]	FF[a] [%]	PCE[b] [%]
Planar control	0.61 ± 0.01	19.8 ± 0.7	57 ± 2	6.9 ± 0.2
Optimized NWN device	0.61 ± 0.01	22.5 ± 0.9	53 ± 2	7.3 ± 0.2

[a]Fill factor (FF); [b]power conversion efficiency (PCE).

(<25% spectral mismatch) solar simulator (ScienceTech). The bias sweep was performed using a Keithley 2400 digital multimeter. The source intensity was measured using a Melles–Griot broadband power meter through a circular aperture of 0.049 cm^2 and set to be 100 mW cm^{-2}. We used an aperture slightly smaller than the top electrode to avoid overestimating the photocurrent: the entire photon fluence passing through the aperture was counted as incident on the device for all analyses of J_{SC} and EQE.[22] The spectral mismatch of the system was characterized using a calibrated reference solar cell (Newport). The total AM1.5 spectral mismatch—taking into account the simulator spectrum and the spectral responsivities of the test cell, reference cell, and broadband power meter—was re-measured periodically and found to be ~11%. This multiplicative factor, M = 0.89, was applied to the current density values of the J–V curve to most closely resemble true AM 1.5 performance.[23] The test cell was mounted in a thermoelectric-cooled holder with temperature feedback. The testing temperature was measured with a thermal couple and stabilized at 25.0 ± 0.1 °C according to the ISO standard. The total accuracy of the AM1.5 power conversion efficiency measurements was estimated to be ± 7%.

TEM, SEM, EDX, and EQE Characterization: For TEM study of the devices and the optimized NWN electrode, thin films (about 100 nm thickness) were prepared using field ion beam milling (Zeiss NVision 40 FIB-SEM, Carl Zeiss Inc., Germany) using a Ga$^+$ beam followed by an argon-ion nano-milling. A high resolution STEM (FEI Titan 80-300 Cubed TEM, FEI, USA) equipped with EDS/EELS analyzers was utilized for imaging. TEM analysis of LPD-treated ZnO NWs was performed using high resolution TEM (JEOL 2010 HRTEM). SEM characterization was obtained on a Hitachi S-5200 scanning electron microscope. Compositional analysis was performed using an energy-dispersive X-ray spectrometer attached to the SEM. The incident spectrum for EQE measurements was generated by a 400 W Xe (Horiba Jobin-Yvon) lamp. The light was passed through a monochromator (Horiba Jobin-Yvon FL-1039), filters (Newport), and an optical chopper operating at 100 Hz coupled to the input of a Stanford Research Systems lock-in amplifier. The collimated light output was measured through a 0.049 cm^2 aperture with calibrated Newport 818-UV and Newport 818-IR power meters. The photogenerated current was measured using a lock-in amplifier. The measurement step was 20 nm and the intensity varied with the spectrum of the Xe lamp.

Capacitance–Voltage Measurement: The capacitance–voltage measurements were performed using an Agilent 4284A LCR meter at a frequency of 10 kHz. The scanning voltage range was −1.0 to 1.0 V.

Supporting Information

Supporting Information is available from the Wiley Online Library or from the author.

[1] E. H. Sargent, *Nat. Photon.* **2012**, *6*, 133.
[2] A. H. MacDonald, P. Schiffer, N. Samarth, *Nat. Mater.* **2005**, *4*, 195.
[3] O. E. Semonin, J. M. Luther, S. Choi, H. Chen, J. Gao, A. J. Nozik, M. C. Beard, *Science* **2011**, *334*, 1530.
[4] A. K. Rath, M. Bernechea, L. Martinez, Pelayo F. Garcia De Arquer, J. Osmond, G. Konstantatos, *Nat. Photon.* **2012**, *6*, 529.
[5] J. Tang, E. H. Sargent, *Adv. Mater.* **2010**, *23*, 12.
[6] J. M. Luther, J.B. Gao, M.T. Lloyd, O.E. Semonin, M.C. Beard, A.J. Nozik, *Adv. Mater* **2010**, *22*, 3704.
[7] B. I. MacDonald, A. Martucci, S. Rubanov, S. E. Watkins, P. Mulvaney, J. J. Jasieniak, *ACS Nano* **2012**, *6*, 5995.

[8] A. H. Ip, S. M. Thon, S. Hoogland, O. Voznyy, D. Zhitomirsky, R. Debnath, L. Levina, L. R. Rollny, G. H. Carey, A. Fischer, K. W. Kemp, I. J. Kramer, Z. Ning, A. J. Labelle, K. W. Chou, A. Amassian, E. H. Sargent, *Nature Nanotech.* **2012**, *7*, 577.

[9] A. G. Pattantyus-Abraham, I. J. Kramer, A. R. Barkhouse, X. Wang, G. Konstantatos, R. Debnath, L. Levina, I. Raabe, M. K. Nazeeruddin, M. Graetzel, E. H. Sargent, *ACS Nano* **2010**, *4*, 3374.

[10] C. H. Henry, *J. Appl. Phys.* **1980**, *51*, 4494.

[11] D. A. R. Barkhouse, I. J. Kramer, X. Wang, E. H. Sargent, *Optics Express* **2010**, *18*, A451.

[12] K. W. Johnston, A. G. Pattantyus-Abraham, J. P. Clifford, S. H. Myrskog, S. Hoogland, H. Shukla, E. J. D. Klem, L. Levina, E. H. Sargent, *Appl. Phys. Lett.* **2008**, *92*, 122111.

[13] D. A. R. Barkhouse, R. Debnath, I. J. Kramer, D. Zhitomirsky, A. G. Pattantyus-Abraham, L. Levina, L. Etgar, M. Grätzel, E. H. Sargent, *Adv. Mater.* **2011**, *23*, 3134.

[14] I. J. Kramer, D. Zhitomirsky, J. D. Bass, P. M. Rice, T. Topuria, L. Krupp, S. M. Thon, A. H. Ip, R. Debnath, H. Kim, E. H. Sargent, *Adv. Mater.* **2012**, *24*, 2315.

[15] M. Law, L. E. Greene, A. Radenovic, T. Kuykendall, J. Liphardt, P. Yang, *J. Phys. Chem. B* **2006**, *110*, 22652.

[16] N. Sakai, N. Kawashima, T. N. Murakami, *Chem. Lett.* **2011**, *40*, 162.

[17] L. E. Greene, M. Law, J. Goldberger, F. Kim, J. C. Johnson, Y. F. Zhang, R. J. Saykally, P. D. Yang, *Angew. Chem. Int. Ed.* **2003**, *42*, 3031.

[18] L. E. Greene, M. Law, D. H. Tan, M. Montano, J. Goldberger, G. Somorjai, P. Yang, *Nano Lett.* **2005**, *5*, 1231.

[19] J. H. Lee, I.C. Leu, M. C. Hsu, Y. W. Chung, M. H. Hon, *J. Phys. Chem. B* **2005**, *109*, 13056.

[20] C. Xu, J. Wu, U. V. Desai, D. Gao, *Nano Lett.* **2012**, *12*, 2420.

[21] H. Liu, J. Tang, I. J. Kramer, R. Debnath, G. I. Koleilat, X. Wang, A. Fisher, R. Li, L. Brzozowski, L. Levina, E. H. Sargent, *Adv. Mater.* **2011**, *23*, 3832.

[22] H. J. Snaith, *Nat. Photon.* **2012**, *6*, 337.

[23] J. M. Kroon, M. M. Wienk, W. J. H. Verhees, J. C. Hummelen, *Thin Solid Films*, **2002**, *223*, 403–404.